Separating the contributions of electric and magnetic fields in deflecting the probes in proton radiography with multiple proton energies

Bao Du,[1] [iD] Hong-Bo Cai,[1,2,3,a] [iD] Wen-Shuai Zhang,[1] [iD] Xiao-Fang Wang,[4] Dong-Guo Kang,[1] [iD] Luan Deng,[5] [iD] En-Hao Zhang,[5] Pei-Lin Yao,[6] [iD] Xin-Xin Yan,[2] Shi-Yang Zou,[1] and Shao-Ping Zhu[1,5,7,a]

AFFILIATIONS

[1]Institute of Applied Physics and Computational Mathematics, Beijing 100094, China
[2]HEDPS, Center for Applied Physics and Technology, Peking University, Beijing 100871, China
[3]IFSA Collaborative Innovation Center, Shanghai Jiao Tong University, Shanghai 200240, China
[4]Department of Engineering and Applied Physics, University of Science and Technology of China, Hefei 230026, China
[5]Graduate School, China Academy of Engineering Physics, Beijing 100088, China
[6]Department of Engineering Physics, Tsinghua University, Beijing 100084, China
[7]STPPL, Research Center of Laser Fusion, China Academy of Engineering Physics, Mianyang 621900, China

[a]Authors to whom correspondence should be addressed: cai_hongbo@iapcm.ac.cn and zhu_shaoping@iapcm.ac.cn

ABSTRACT

In proton radiography, degeneracy of electric and magnetic fields in deflecting the probe protons can prevent full interpretation of proton flux perturbations in the detection plane. In this paper, theoretical analyses and numerical simulations suggest that the contributions of the electric and magnetic fields can be separately obtained by analyzing the difference between the flux distributions of two discriminated proton energies in a single shot of proton radiography. To eliminate the influence of field evolution on the separation, a strategy is proposed in which slow field evolution is assumed or an approximate estimate of field growth is made. This could help achieve a clearer understanding of the radiographic process and allow further quantitative analysis.

I. INTRODUCTION

For plasma physics related to inertial confinement fusion,[1] laboratory astrophysics,[2] and particle acceleration based on laser–plasma interactions,[3] the electric field E and magnetic field B are of fundamental importance. Accurate experimental measurement of E and B fields is a basic demand in requirement in these and related areas.

Proton radiography is a commonly used experimental method to image the structures of E and B fields inside plasmas.[4–7] In recent decades, it has helped in the development or confirmation of many theories relating to E and B fields in plasma physics.[8–11] The general scheme of proton radiography of E and B fields can be described as follows.[12–14] A proton beam is emitted from a source and traverses the field to be imaged almost in parallel. The probe protons are deflected by the E or B field (or both) and acquire a deflection velocity u_d perpendicular to the initial velocity u_0. After traversing the field region, the probe protons return to free flight and are deposited on a two-dimensional (2D) detection plane. When the distance L_D between the detection plane and the field region is large enough, the spatial distributions of u_d finally bring about an observable flux density perturbation of the probe protons $\delta n/n_0 = n/n_0 - 1$, where n and n_0 are the flux densities in the presence and absence of the fields, respectively. When a radiochromatic film (RCF) stack is used as the proton flux detector, protons of different kinetic energies will be deposited on separate RCF layers.[15] Such energy resolution can also be achieved when CR-39 polymer is used as the detector. $\delta n/n_0$ can then be used to indicate the spatial distribution of the E or B field. With an appropriate reconstruction algorithm, characteristic values or the spatial structure of the field can be reconstructed from $\delta n/n_0$ in some situations.[12,14,16]

Before carrying out a further analysis of $\delta n/n_0$ obtained from the proton detector, we first need a quantitative separation (or at least a qualitative distinction) of the contributions from the E and B fields. However, the E field and B field can cause substantial deflections of the probe protons, it is hard to judge from the proton detector whether $q\int E\,ds$ or $q\int u_0\times B\,ds$ is the dominant source in forming the detected $\delta n/n_0$ (where s is a unit length along the proton trajectory). This prevents one from obtaining a qualitative understanding of the properties of the imaged field, not to mention a quantitative reconstruction. The situation can become even more confusing when E and B fields coexist in a plasma and deflect the probe protons in the same directions and with comparable contributions. For example, in the widely studied side-on proton radiography of a laser-ablated solid target, the azimuthal B field generated through the Biermann battery effect and the longitudinal E field generated by the plasma sheath can both deflect probe protons in the same longitudinal direction.[17]

In previous studies, the problem of distinguishing between E and B fields in proton radiography has frequently been dealt with by assuming that one of the two fields can be ignored, with the choice being made mainly on the basis of particle-in-cell (PIC) simulations or experimental experience.[5,10,16] For example, in the proton radiography of a capacitor–coil B field generator, the E field is believed to have no impact on the proton trajectory because a large number of simulations and theoretical studies have shown that no E field can be generated at the center of the coil.[18] However, in the proton radiography of plasmas, which is most relevant to high-energy and high-density physics, E and B fields generally coexist. In many situations, neither numerical simulations nor appropriate theoretical models are available. Research by Li et al.[1] and Huntington et al.[2] suggest that deflections due to the B field are inversely proportional to the square root of the proton energy, while those due to the E field are inversely proportional to the proton energy. Thus, by using D–D and D–^{3}He fusion protons as probes, the dominant field in deflecting the protons can be determined. However, such studies can only provide a qualitative judgement, and a rough assumption in which either the E field or the B field is ignored must still be made before field reconstruction can be performed or the obtained $\delta n/n_0$ can be understood.[4,5,10] To obtain a clear and rigorous reconstruction, a method to realize quantitative separation of the contributions of the E and B fields in forming the diagnosed $\delta n/n_0$ on the detection plane needs to be developed. However, to the best of our knowledge, such a method has yet to be reported in the open literature.

In this paper, we find that when RCF stacks or CR-39 polymer are used as proton detectors to resolve the energy of the probe protons, the path integrals of the E and B fields can be separately reconstructed from the proton radiography by analyzing the difference in $\delta n/n_0$ between two discriminated proton energies in a single shot.

II. THEORY OF SEPARATE RECONSTRUCTION

When E and B fields coexist in proton radiography, the deflection velocity of the probe proton beam at its exit from the field region can be written as

$$u_d \approx \frac{q}{\gamma m_p}\int (E+u_0\times B)\frac{dx}{u_0} \approx \frac{q}{m_p}\int\left(\frac{E}{u_0}+e_x\times B\right)dx, \quad (1)$$

where q, m_p, and γ are the proton charge, mass, and relativistic factor, respectively. $\gamma\approx 1$ is assumed here because for proton radiography as commonly applied, the probe protons are generated either through a target normal sheath acceleration (TNSA) mechanism or through D–D and D–^{3}He implosions, and the kinetic energy is rather small compared with the rest energy.[1–3] The probe protons are assumed to be emitted in the x direction, $u_0 = u_0 e_x$. It is clear from Eq. (1) that to distinguish between the E and B fields in the formation of the deflection velocity u_d, the most direct method is to reconstruct $\int E\,dx$ and $\int e_x\times B\,dx$ separately but simultaneously in a single radiographic observation.

For two discriminated proton energies, we can assume that the corresponding proton initial velocities are $u_0 = u_1 = u_1 e_x$, and $u_0 = u_2 = u_2 e_x$. When these protons pass through the field region, the deflection velocities are respectively

$$u_{d1} = \frac{q}{m_p}\int\left(\frac{E}{u_1}+e_x\times B\right)dx, \quad (2)$$

$$u_{d2} = \frac{q}{m_p}\int\left(\frac{E}{u_2}+e_x\times B\right)dx. \quad (3)$$

From a comparison between these expressions, the path integrals of the E and B fields can be obtained as follows:

$$(2)-(3)\Rightarrow \int E\,dx = \frac{m_p}{q}(u_{d1}-u_{d2})\frac{u_1 u_2}{u_2-u_1}, \quad (4)$$

$$u_1(2)-u_2(3)\Rightarrow \int e_x\times B\,dx = \frac{m_p}{q}(u_1 u_{d1}-u_2 u_{d2})\frac{1}{u_1-u_2}. \quad (5)$$

Thus, if the deflection velocities of the probe protons with discriminated energies, namely, u_{d1} and u_{d2}, can be reconstructed from the proton radiography, then the path integrals of the E and B fields can be separately obtained in a single shot.

In proton radiography, when the linearity requirement $\delta n/n_0 < 1$ is satisfied, crossing or overlapping of the trajectories of the probe protons can be avoided. The deflection velocities u_{d1} and u_{d2} can be reconstructed as[12,19]

$$u_{d1} = -\frac{u_1 M}{L_D}\int\left(\frac{\delta n}{n_0}\right)_1 dl, \quad (6)$$

$$u_{d2} = -\frac{u_2 M}{L_D}\int\left(\frac{\delta n}{n_0}\right)_2 dl, \quad (7)$$

where $M = L_D/L_S + 1$ is the magnification factor, and l is parallel to the deflection velocity, which can be seen most clearly from the detected $\delta n/n_0$. Equations (6) and (7) provide a convenient reconstruction of the one- or two-dimensional deflection velocity in one direction of deflection. However, in experimental applications, the deflection direction l at a given spatial position may be hard to judge when $\delta n/n_0$ has a complicated form. Nevertheless, for many situations where $\delta n/n_0$ exhibits parallel structures, the local deflection direction l can be easily inferred to be one-dimensional and normal to these parallel structures when $\delta n/n_0 < 1$ is satisfied to ensure a local deflection. For example, in applications of proton radiography to collisionless

shocks,[20] plasma jets,[7] or sheath fields,[19] the deflection direction can be found from the experimentally obtained $\delta n/n_0$ stripes. In this paper, to obtain a good reconstruction of the deflection velocity, L_D is varied in different situations to meet the linearity requirement $\delta n/n_0 < 1$.[11,12,19] $(\delta n/n_0)_{1,2}$ correspond to the probe flux density perturbations at the same areas for two discriminated proton energies, and L_D and L_S are the distances from the field region to the detector and proton source, respectively. In more complex situations where the deflection direction is hard to determine from the detected $\delta n/n_0$, the use of Eq. (6) or (7) may not be appropriate for reconstructing the deflection velocities. In such cases, the approach of Bott et al.[14] of numerically solving a Monge–Ampère equation for $\delta n/n_0$ is advised. This Monge–Ampère method can give a global reconstruction of the two-dimensional deflection velocity in two directions, although this requires an undisturbed boundary of $\delta n/n_0$ where deflections from the $\boldsymbol{E}$ and $\boldsymbol{B}$ fields or particle scattering are not allowed to be imposed on the probe protons. This condition may not be satisfied in some situations because of sheltering by the target holder and the target itself or a nonuniform spatial distribution of the proton source. In reconstructing the deflection velocity, the choice of whether to use Eqs. (6) and (7) or the Monge–Ampère method should be flexible and based on specific practical needs.

Then, by individually reconstructing $\boldsymbol{u}_{d1}$ and $\boldsymbol{u}_{d2}$ from the detected $\delta n/n_0$, the contributions of the $\boldsymbol{E}$ and $\boldsymbol{B}$ fields to the deflection of the probe protons, i.e., $\int \boldsymbol{E}\, dx$ and $\int \boldsymbol{e}_x \times \boldsymbol{B}\, dx$, can be characterized with Eqs. (4) and (5).

III. BENCHMARK SIMULATION

To prove that the theoretical approach described in Sec. II is able to distinguish the $\boldsymbol{E}$ and $\boldsymbol{B}$ fields in proton radiography, a benchmark simulation is demonstrated here.
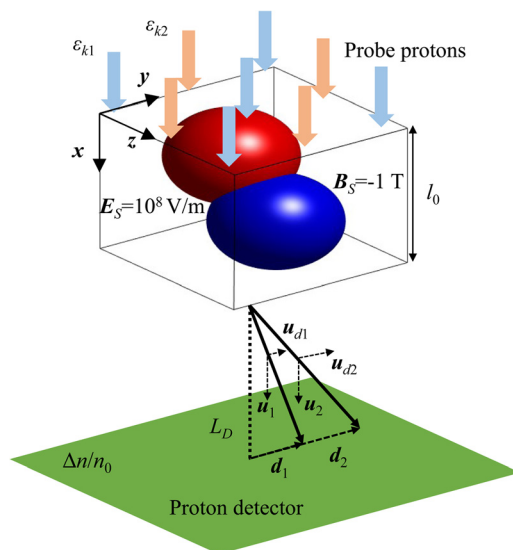

FIG. 1. Geometry of the radiography of $\boldsymbol{E}$ and $\boldsymbol{B}$ fields with protons of multiple energies. The field region contains isosurfaces of the $\boldsymbol{E}$ and $\boldsymbol{B}$ fields at $E_s = 10^8$ V/m and $B_s = -1$ T.

In this simulation, a probe proton beam is emitted for radiography of a 3D field box of $(L_0 = 100\ \mu m)^3$, in which $\boldsymbol{E}$ and $\boldsymbol{B}$ fields coexist and are static. The $\boldsymbol{E}$ field is in the y direction with a spatial distribution $\boldsymbol{E} = E_0 \exp\{-[(x - x_{0E})^2 + (z - z_{0E})^2 + (y - y_0)^2]/R_0^2\}\boldsymbol{e}_y$, with $E_0 = 5 \times 10^8$ V/m. The $\boldsymbol{B}$ field is in the z direction with a 3D spatial distribution $\boldsymbol{B} = -B_0 \exp\{-[(x - x_{0B})^2 + (z - z_{0B})^2 + (y - y_0)^2]/R_0^2\}\boldsymbol{e}_z$, with $B_0 = 5$ T. Here, $(x_{0E}, z_{0E}, y_0) = (L_0/3, L_0/3, L_0/2)$, $(x_{0B}, z_{0B}, y_0) = (2L_0/3, 2L_0/3, L_0/2)$, and $R_0 = L_0/3$. Beyond the edges of the simulation box, the $\boldsymbol{E}$ and $\boldsymbol{B}$ fields have nonzero values, but will not influence the simulation or reconstruction. The isosurfaces of $E_s = 10^8$ V/m and $B_s = -1$ T plotted in Fig. 1 can help to determine the spatial distributions of the $\boldsymbol{E}$ and $\boldsymbol{B}$ fields in our simulation. The proton trajectories under deflection by the pre-set $\boldsymbol{E}$ and $\boldsymbol{B}$ fields are calculated using a Runge–Kutta method, while outside the field region, the protons are assumed to undergo free flight.

The probe protons pass in parallel through the field region in the x direction. Both the $\boldsymbol{E}$ and $\boldsymbol{B}$ fields will deflect the probe protons in the same (y) direction. After being deflected in the field region and undergoing free flight for $L_D = 2$ cm, the flux density perturbations $\delta n/n_0$ of the probe protons are obtained in the detection plane, as shown in Fig. 2. $\delta n/n_0$ in Figs. 2(a) and 2(b) correspond to protons of initial kinetic energies $\varepsilon_{k1} = 20$ MeV ($u_1 = 6.1 \times 10^7$ m/s) and $\varepsilon_{k2} = 40$ MeV ($u_2 = 8.5 \times 10^7$ m/s), respectively.[21] In experimental proton radiography, such an energy resolution can be conveniently achieved by using RCF stacks or CR-39 as the proton detector. Clearly, for both flux density perturbations corresponding to $\varepsilon_{k1} = 20$ MeV and $\varepsilon_{k2} = 40$ MeV, $\delta n/n_0 < 1$ is satisfied, which indicates that crossing or overlapping of proton trajectories is prevented.[12,19] This allows us to reconstruct the deflection velocities u_{d1} and u_{d2} through Eqs. (6) and (7). The deflection velocities for protons of $\varepsilon_{k1} = 20$ MeV and $\varepsilon_{k2} = 40$ MeV, reconstructed from $\delta n/n_0$ in Figs. 2(a) and 2(b), are shown in Figs. 2(c) and 2(d), respectively. Differences between $(\delta n/n_0)_1$ and $(\delta n/n_0)_2$ (and between the corresponding reconstructed u_{d1} and u_{d2}) can clearly be seen in Fig. 2. These result from the differences between the $\boldsymbol{E}$ and $\boldsymbol{B}$ fields in responding to the proton kinetic energy. The difference between $(\delta n/n_0)_1$ and $(\delta n/n_0)_2$ is key to realizing the separation or reconstruction of $\int \boldsymbol{E}\, dx$ and $\int \boldsymbol{e}_x \times \boldsymbol{B}\, dx$.

Using Eqs. (4) and (5), the path integrals of the $\boldsymbol{E}$ and $\boldsymbol{B}$ fields are reconstructed from u_{d1} and u_{d2} as shown in Fig. 3. In Figs. 3(a) and 3(b), the 2D spatial distributions of $\int \boldsymbol{E}\, dx$ exhibit good agreement between the reconstructed and pre-set structures. The more quantitative 1D comparison in Fig. 3(c) further indicates that $\int \boldsymbol{E}\, dx$ is reconstructed well from the proton radiography. This means that the contribution of the $\boldsymbol{E}$ field in deflecting the probe protons can be separately obtained by analyzing the flux density perturbations corresponding to two discriminated proton energies. At the same time, the 2D and 1D comparisons of $\int \boldsymbol{B}\, dx$ in Figs. 3(d)–3(f) suggest that the contribution of the $\boldsymbol{B}$ field in deflecting the probe protons is also reconstructed well from the same detected proton fluxes. Thus, it is shown by the above benchmark simulations that $\int \boldsymbol{E}\, dx$ and $\int \boldsymbol{B}\, dx$ can be reconstructed separately and simultaneously in a single radiographic observation with different kinetic energies of the probe protons.

We should also mention that for protons of kinetic energy at the MeV level (as is the situation in our simulation and most proton radiography with a TNSA, D–D, or D–^{3}He implosion proton
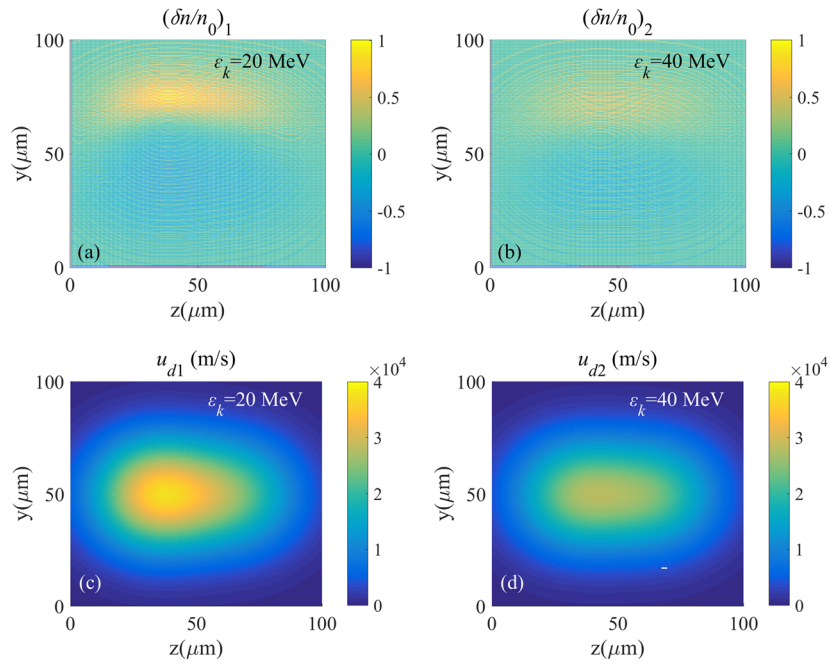
FIG. 2. (a) and (b) Spatial distributions of flux density perturbations $(\delta n/n_0)_1$ and $(\delta n/n_0)_2$ in the detection plane during radiography of the fields shown in Fig. 1 with protons in parallel, corresponding to protons of $\varepsilon_{k1} = 20$ MeV and $\varepsilon_{k2} = 40$ MeV, respectively. (c) and (d) Reconstructed spatial distributions of the deflection velocities u_{d1} and u_{d2} corresponding to protons of $\varepsilon_{k1} = 20$ MeV and $\varepsilon_{k2} = 40$ MeV, respectively.

FIG. 3. (a) and (b) 2D distributions of the reconstructed and pre-set $\int E\, dx$, respectively; (c) 1D comparison of these distributions along $y = 0$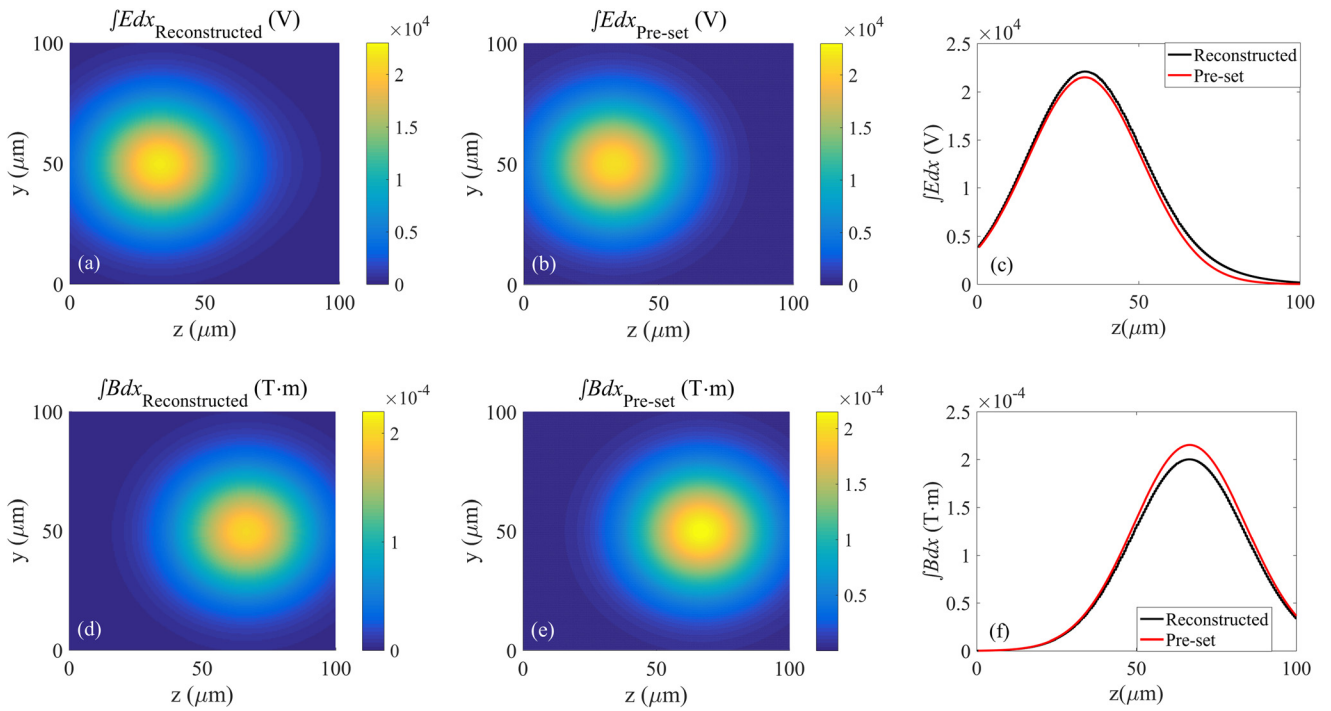. (d) and (e) 2D distributions of the reconstructed and pre-set $\int B\, dx$, respectively; (f) 1D comparison of these distributions along $y = 0$.

source[1–3]), the strengths of the E and B fields in this benchmark simulation are specially chosen to make a comparable contribution to the deflection of the probe protons and thus allow an examination of the performance of the demonstrated distinguishing method. The spatial locations of the E and B fields also partially overlap with each other. This means that the E and B fields can be substituted for one another to some extent when deflecting the probe protons, both in terms of spatial distribution and deflection force. It is therefore impossible to distinguish the contributions of the E and B fields in forming the probe flux density with a given proton energy. This further highlights the capability of the method presented here.

It is necessary to address a technical problem here, namely, that an ideal resolution of proton kinetic energy is hard to achieve in experiments when RCF stacks are used for proton detection. For an RCF layer, the deposited energy comes predominantly from protons that die in it. However, when a proton with higher energy passes through, it will also make a contribution. The deposited energy cannot come entirely from protons of a specific kinetic energy. If the protons are generated by TNSA, there will be a falling exponential tail.[22] As a result, when using TNSA protons as the probe, RCF layers corresponding to higher proton energies should be used in the separating reconstruction to reduce the influence of energy resolution. Otherwise, it is preferable to use D–D and D–^{3}He fusion protons as the probe, since these have a much narrower spectral width compared with TNSA protons, provided that the temporal blurring effect caused by proton pulse duration is negligible.[6]

IV. ELIMINATING THE INFLUENCE OF FIELD EVOLUTION

Before applying the above method to analyze the proton flux density obtained from a radiography experiment, there is an important issue that should be emphasized. In the theory and simulations described above, the main way in which the E and B fields are distinguished is through the difference in how they respond to the proton velocity. The benchmark demonstration has shown how it is possible to distinguish between the E and B fields by using RCF stacks or CR-39 as the detector to resolve the proton velocity. However, the fields in our benchmark simulation are static. In a more realistic proton radiography experiment, temporal evolution of the E or B field is unavoidable.[7] Meanwhile, after being emitted from the source, the probe protons will enter the field region at different times. The difference between the flux density distributions of protons with two discriminated energies could possibly come from the temporal evolution of the E and B fields themselves when they are fast evolving.[20] There is thus competition between the probe energy disparity and the field evolution in their effects on the difference between $(\delta n/n_0)_1$ and $(\delta n/n_0)_2$.

Suppose that the E and B fields during the passage of protons with a kinetic energy ε_{k1} are increased by a factor of $f_{E,B}$ compared with their values for a higher kinetic energy ε_{k2}, i.e., $(E)_1 = (1 + f_E)(E)_2$ and $(B)_1 = (1 + f_B)(B)_2$. Physically, $f_{E,B}$ is directly connected with the growth rate of the E and B fields and the distance L_S from the proton source to the field region. Suppose that the growth rates of the fields are

$$\eta_{E,B} = \frac{1}{(E,B)} \frac{d(E,B)}{dt}.$$

Then, $f_{E,B}$ can be written as $f_{E,B} = \eta_{E,B}\Delta t$, where $\Delta t = L_s(1/u_1 - 1/u_2)$ is the gap between the arrival times of the higher- and lower-energy

protons in the field region. When $f_{E,B}$ is constant and set as 0.2, $\int E \, dx$ and $\int e_x \times B \, dx$ are reconstructed with different probe energies. Following the same steps as in Sec. III, 1D distributions of the reconstructed $\int E \, dx$ and $\int e_x \times B \, dx$ along $y = 0$ are shown in Figs. 4(a) and 4(b), respectively. The amplitudes of the reconstructed $\int E \, dx$ and $\int e_x \times B \, dx$ are ~50% higher and 30% lower than the pre-set values, respectively. The spatial shapes are also altered, depending on $f_{E,B}$, especially for the B field. When the gap between ε_{k1} and ε_{k2} is larger, the reconstructed fields will be closer to the pre-set ones. Figures 5(a) and 5(b) show 1D distributions of the reconstructed $\int E \, dx$ and $\int e_x \times B \, dx$, respectively, along $y = 0$ at different values of $f_{E,B}$. The proton kinetic energies are $\varepsilon_{k1} = 10$ MeV and $\varepsilon_{k2} = 40$ MeV. It can be seen from Figs. 5(a) and 5(b) that the more rapid the evolutions of the E and B fields, the greater is the difference between the reconstructed and pre-set $\int E \, dx$ and $\int e_x \times B \, dx$. When $f_{E,B} = 0.4$, the amplitudes of the reconstructed $\int E \, dx$ and $\int e_x \times B \, dx$ are respectively two times higher and 50% lower than the pre-set values. Clearly, only in proton radiography of slowly evolving E and B fields will the distinguishing method demonstrated above exhibit good performance.

In spite of the competition between the probe energy disparity and the field evolution in determining the difference between $(\delta n/n_0)_1$ and $(\delta n/n_0)_2$, it should be noted that with different ε_{k1} and ε_{k2}, Δt will also be changed. This means that ε_k itself will have an influence on $f_{E,B}$. Figures 5(c) and 5(d) show the differences between the reconstructed fields E_R, B_R, and pre-set fields E_P, B_P, at $z = 50$ μm for different values of the growth rate η. η_0 is the field growth rate corresponding to $f_{E,B} = 0.1$ for $\varepsilon_{k1} = 30$ MeV, $\varepsilon_{k2} = 40$ MeV, and $L_s = 1$ cm. It can be seen that for a given growth rate, when the probe energy disparity is increased, the difference between the reconstructed and pre-set fields will also increase. This suggests that to achieve accurate reconstruction and separation of the E and B fields, a shorter distance from the proton source to the field region and a smaller gap between ε_{k1} and ε_{k2} should be adopted.

Nevertheless, we have come up with a strategy to overcome the influence of field evolution on distinguishing between E and B fields, and this has been proved to greatly improve the performance of the above method. In fact, for many studies in plasma physics, assumptions regarding the conservation of electric and magnetic field energy can be made.[23,24] In other situations, the temporal growth rates of E and B fields can be estimated through theoretical analyses or PIC simulations.[25] Therefore, before using Eqs. (4) and (5) for reconstruction, an approximate estimation of f_{E0} and f_{B0} can be conducted. Thus, the deflection velocities of lower-energy (ε_{k1}) and higher-energy (ε_{k2}) protons are

$$u_{d1} \approx \frac{q}{m_p} \int \left[\frac{(1 + f_{E0})E}{u_1} + e_x \times (1 + f_{B0})B \right] dx, \qquad (8)$$

$$u_{d2} \approx \frac{q}{m_p} \int \left(\frac{E}{u_2} + e_x \times B \right) dx, \qquad (9)$$

respectively. The path integrals of the E and B fields then can be reconstructed as follows:

$$(8) - (1 + f_{B0})(9) \Rightarrow \int E \, dx$$
$$= \frac{m_p}{q} \frac{u_1 u_2 [u_{d1} - (1 + f_{B0})u_{d2}]}{(1 + f_{E0})u_2 - (1 + f_{B0})u_1}, \qquad (10)$$
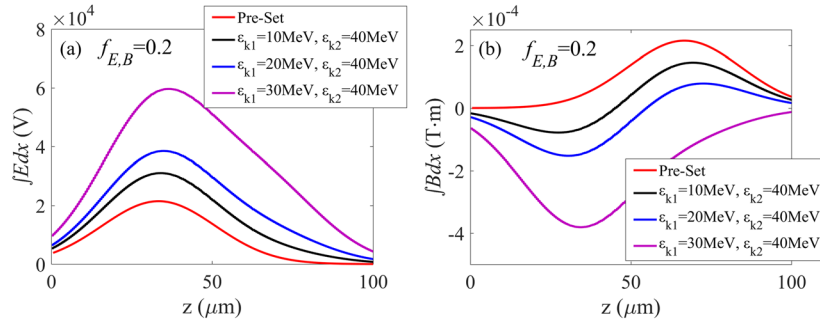
FIG. 4. If the field imaged with lower-energy probe protons is changed by a given factor of $f_{E,B} = 0.2$ compared with that imaged with higher-energy probes, the reconstructed (a) $\int \boldsymbol{E}\, dx$ and (b) $\int \boldsymbol{e}_x \times \boldsymbol{B}\, dx$ will be closer to the pre-set distributions when the energy gap $\varepsilon_{k2} - \varepsilon_{k1}$ is larger.

$$u_1(8) - u_2(1 + f_{E0})(9) \Rightarrow \int \boldsymbol{e}_x \times \boldsymbol{B}\, dx$$
$$= \frac{m_p}{q} \frac{[u_1 \boldsymbol{u}_{d1} - (1 + f_{E0}) u_2 \boldsymbol{u}_{d2}]}{(1 + f_{B0}) u_1 - (1 + f_{E0}) u_2}. \qquad (11)$$

In this way, when f_{E0} and f_{B0} are estimated as close as to the actual f_E and f_B, the influence of field evolution can be eliminated in the reconstruction. In Fig. 6, the strengths of $\boldsymbol{E}$ and $\boldsymbol{B}$ fields through which protons of $\varepsilon_{k1} = 30$ MeV pass are $f_E = f_B = 0.5$ times larger than those for protons of $\varepsilon_{k1} = 40$ MeV. Without the fix described above, the

$\int \boldsymbol{E}\, dx$ and $\int \boldsymbol{e}_x \times \boldsymbol{B}\, dx$ reconstructed using Eqs. (4) and (5), and shown as the black lines in Fig. 6, are respectively about 4.4 and 3.7 times larger than the pre-set values, shown as the red lines. When the fix is adopted and $f_{E0} = f_{B0} = 0.5$ are estimated, the $\int \boldsymbol{E}\, dx$ and $\int \boldsymbol{e}_x \times \boldsymbol{B}\, dx$ reconstructed using Eqs. (10) and (11), and shown as the blue lines in Fig. 6, both agree well with the pre-set values. Even if f_{E0} and f_{B0} are over- or under-estimated, a clear correction to the reconstruction can be achieved, and the influence of field evolution can be largely eliminated. This can be seen by comparing the black lines in Fig. 6 with the green and brown lines, which correspond to an underestimate $f_{E0,B0} = 0.4$ and an over-estimate $f_{E0,B0} = 0.6$, respectively.
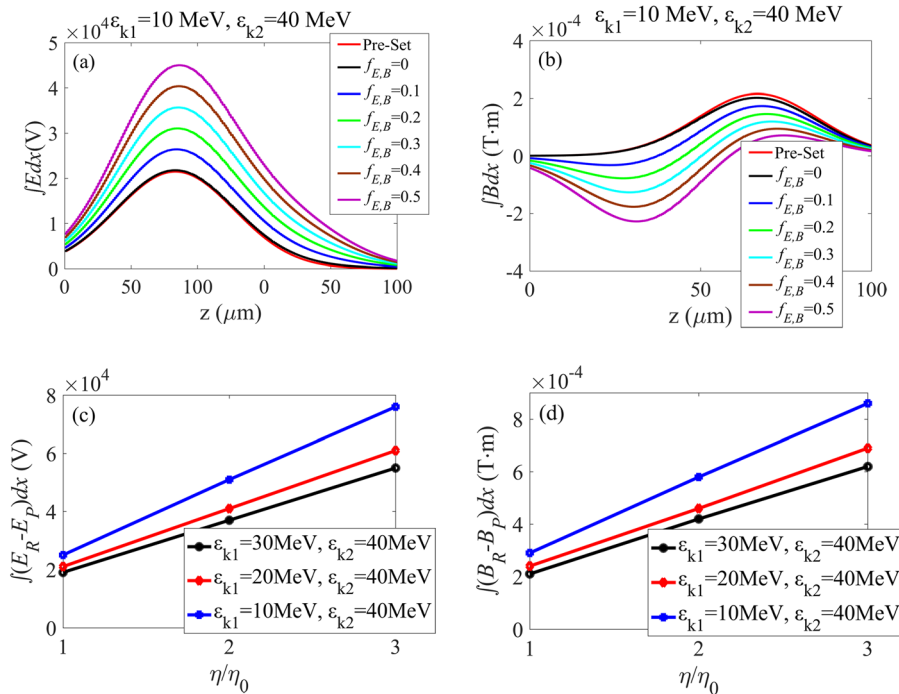

FIG. 5. (a) and (b) There will be differences between the reconstructed and preset $\int \boldsymbol{E}\, dx$ and $\int \boldsymbol{e}_x \times \boldsymbol{B}\, dx$ if the field imaged with lower-energy probes is changed by a factor of $f_{E,B}$ compared with that imaged with higher energy probes. (c) and (d) Difference between the reconstructed and pre-set fields at $z = 50\ \mu m$ for different values of the field growth rate η: (c) $\int (\boldsymbol{E}_R - \boldsymbol{E}_P)\, dx$; (d) $\int (\boldsymbol{B}_R - \boldsymbol{B}_P)\, dx$. This indicates that for larger $\varepsilon_{k1} - \varepsilon_{k2}$, the reconstructed fields will differ more from the pre-set fields.
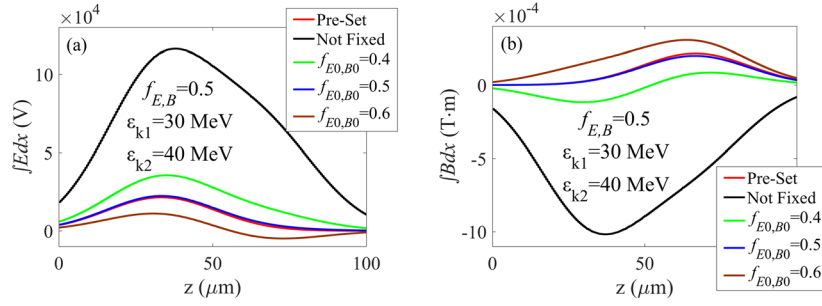
FIG. 6. When $f_{E,B}$ are estimated as $f_{E0,B0}$, the difference between the pre-set distributions and the reconstructed (a) $\int \boldsymbol{E}\,dx$ and (b) $\int \boldsymbol{e}_x \times \boldsymbol{B}\,dx$ can be largely eliminated.

It should be mentioned that when the field is varying, the image itself will be blurred or averaged over the sampling period. TNSA protons are mainly generated by a laser pulse within a duration of about $\tau \approx 1$ ps. The time gap for the higher- and lower-energy protons on their arrival at the field region is $\Delta t = L_s(1/u_1 - 1/u_2)$. Assume a regular source distance of $L_s = 1$ cm and that u_1 and u_2 correspond to kinetic energies of 20 MeV and 40 MeV. Then, $\Delta t \approx 46$ ps, which is far larger than the pulse duration $\tau \approx 1$ ps. If the imaged field is increased or reduced by 100% during the gap of imaging time of the higher- and lower-energy protons, the field evolution during the pulse duration will be about 2%. In considering the influence of field evolution on the separation, the pulse duration can be ignored in comparison with the imaging time gap. However, for D–D and D–^{3}He nuclear fusion protons, which are generated in ablation by nanosecond lasers, the pulse duration can be larger than 100 ps.[1] Also, for protons in a given RCF layer, a bandwidth of at least 1.5 MeV means a blurring time of about 5.8 ps for 20 MeV protons and a 1 cm source distance.[21] For lower-energy protons, this blurring time will be larger. The fields imaged by a given proton beam could undergo obvious changes during the proton passage time. In such a situatios, the deflection velocities can be written as

$$\boldsymbol{u}_{d1} \approx \frac{q}{m_p} \int \left[\frac{\boldsymbol{E}_1(t)}{u_2} + \boldsymbol{e}_x \times \boldsymbol{B}_1(t) \right] dx,$$

$$\boldsymbol{u}_{d2} \approx \frac{q}{m_p} \int \left[\frac{\boldsymbol{E}_2(t)}{u_2} + \boldsymbol{e}_x \times \boldsymbol{B}_2(t) \right] dx.$$

According to the method used in deriving Eqs. (4) and (5) or Eqs. (10) and (11), it can be seen that to separately reconstruct the path integrals of the $\boldsymbol{E}$ or $\boldsymbol{B}$ fields, connections must be found between $\boldsymbol{E}_1(t)$ and $\boldsymbol{E}_2(t)$, as well as between $\boldsymbol{B}_1(t)$ and $\boldsymbol{B}_2(t)$. If these connections cannot be confirmed or even estimated, then the field separation method will fail. For the simplest situation when the field is static, $\boldsymbol{E}_1(t) = \boldsymbol{E}_2(t) = \boldsymbol{E}$ and $\boldsymbol{B}_1(t) = \boldsymbol{B}_2(t) = \boldsymbol{B}$, which is the benchmark case in Sec. III.

It can be seen from $f_{E,B} = \eta_{E,B}\Delta t$ that for a smaller source–field distance L_S or field growth rate $\eta_{E,B}$, $f_{E,B}$ can be reduced. This indicates that in experimental applications, a shorter L_S should be used. However, when neither the slow-evolution assumption can be satisfied nor an approximate estimation of $f_{E0,B0}$ obtained, we believe that the proposed method will fail to separate the contributions of $\boldsymbol{E}$ and $\boldsymbol{B}$ fields in forming the detected proton flux distribution. In such

situations, synthetic simulations of proton radiography or further theoretical analyses must be performed to help to understand the radiography experiment.

V. DISCUSSION

In Sec. II, Eqs. (4) and (5) were deduced by subtracting Eq. (2) from Eq. (3). However, when one of the two terms $\boldsymbol{E}$ and $\boldsymbol{u}_0 \times \boldsymbol{B}$ is clearly dominant over the other, the numerical errors in the subordinate term may fail in competition with the numerical errors in the dominant term in such subtractions., and consequently it will not be possible to reconstruct the subordinate term satisfactorily. This can be seen in the following demonstration of distinguishing the spontaneous $\boldsymbol{E}$ and $\boldsymbol{B}$ fields of a current filamentary instability.

Current filamentary instability, which has been widely studied in the case of counter-streaming plasma flows, generates $\boldsymbol{E}$ and $\boldsymbol{B}$ fields in both longitudinal and transverse directions with respect to the plasma flow with quite complex filamentary structures. Our previous studies have shown that in side-on radiography of such fields, the $\boldsymbol{E}$ field plays the dominant role in deflecting the probe protons in comparison with the $\boldsymbol{B}$ field. In this section, side-on proton radiography with the same imaging layout and PIC simulations of the spontaneous fields in accordance with Ref. 16 are applied. Probe protons are emitted in the x direction to pass through the field region and are deflected in both the y and z directions. The strengths of the $\boldsymbol{E}$ and $\boldsymbol{B}$ fields are reduced by a factor of 10 compared with Ref. 16 to ensure that the probe protons follow straight trajectories inside the field region. The distance from the detection plane to the field region is $L_D = 1$ mm.

For proton beams of kinetic energies $\varepsilon_{k1} = 20$ MeV and $\varepsilon_{k2} = 40$ MeV, the flux density perturbations $(\delta n/n_0)_{1,2}$ in the detection plane are shown in Figs. 6(a) and 6(b), respectively. Because the probe protons are deflected not only in the y direction but also in the z direction, Eqs. (6) and (7) are not applicable for accurately reconstructing the deflection velocity from the obtained $\delta n/n_0$ in Fig. 7. Instead, by following the method of Bott *et al.*[14] and numerically solving a Monge–Ampère equation for $\delta n/n_0$, the deflection velocities in both the y and z directions, $(u_{dy})_{1,2}$ and $(u_{dz})_{1,2}$, can be reconstructed, as shown in Figs. 8(b) and 8(d) for $\varepsilon_{k1} = 20$ MeV and in Figs. 9(b) and 9(d) for $\varepsilon_{k2} = 40$ MeV. More detailed information about the reconstruction method for u_d can be found in Ref. 14. For comparison, the spatial distributions of $(u_{dy})_{1,2}$ and $(u_{dz})_{1,2}$ directly obtained from the radiography simulation at $L_D = 0$ are also shown: see Figs. 8(a) and 8(c) for ε_{k1}, and Figs. 9(a) and 9(c) for ε_{k2}. In this paper, "directly obtained" means that the parameter is obtained
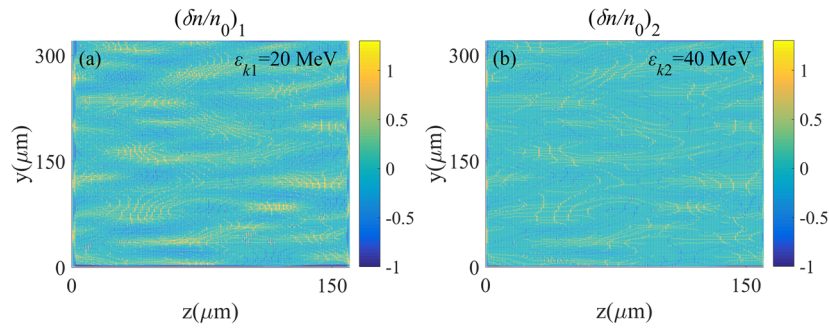
FIG. 7. $\delta n/n_0$ in the detection plane in the proton radiography of a current filamentary instability for (a) $\varepsilon_{k1} = 20$ MeV and (b) $\varepsilon_{k2} = 40$ MeV.

directly or corrected *a priori*, rather than being obtained from the reconstruction.

For $\varepsilon_{k1} = 20$ MeV, a comparison between Figs. 8(a) and 8(b) indicates that the spatial structures of u_{dy1} are reconstructed well from the $(\delta n/n_0)_1$ in the detection plane. Further 1D comparisons of u_{dy1} along $z = 80$ μm and u_{dz1} along $y = 160$ μm can provide a more quantitative evaluation. However, it is obvious that numerical errors exist between the reconstructed u_{dy1} and that directly obtained at $L_D = 0$. Similar numerical errors in the reconstruction are also found for u_{dz1}. For probe protons of $\varepsilon_{k2} = 40$ MeV, the same conclusion can be drawn that deflection velocities are reconstructed well in principle although with clear numerical errors.

With the reconstructed $(u_{dy})_{1,2}$ in Fig. 8(b) for $\varepsilon_{k1} = 20$ MeV and in Fig. 9(b) for $\varepsilon_{k2} = 40$ MeV, $\int E_y\,dx$ can be obtained through Eq. (4); see Fig. 10(a). For comparison, $\int E_y\,dx$ directly obtained from the PIC simulation is also shown in Fig. 10(b). A quantitative 1D comparison is shown in Fig. 10(c). Correspondingly, for $\int E_z\,dx$, the reconstructed results from $(u_{dz})_{1,2}$ in Figs. 8(e) and 9(e) are shown in Fig. 10(d). 2D and 1D comparisons are shown in Figs. 10(e) and 10(f). Clearly, in both the y and z directions, the 2D comparisons of spatial structures and the 1D comparisons of quantitative distributions both suggest that $\int \boldsymbol{E}\,dx$ is reconstructed well from proton radiography.

Similar to the $\boldsymbol{E}$ field, $\int B_z\,dx$ and $\int B_y\,dx$ can also be reconstructed through Eq. (5) with $(u_{dy})_{1,2}$ and $(u_{dz})_{1,2}$, respectively, and
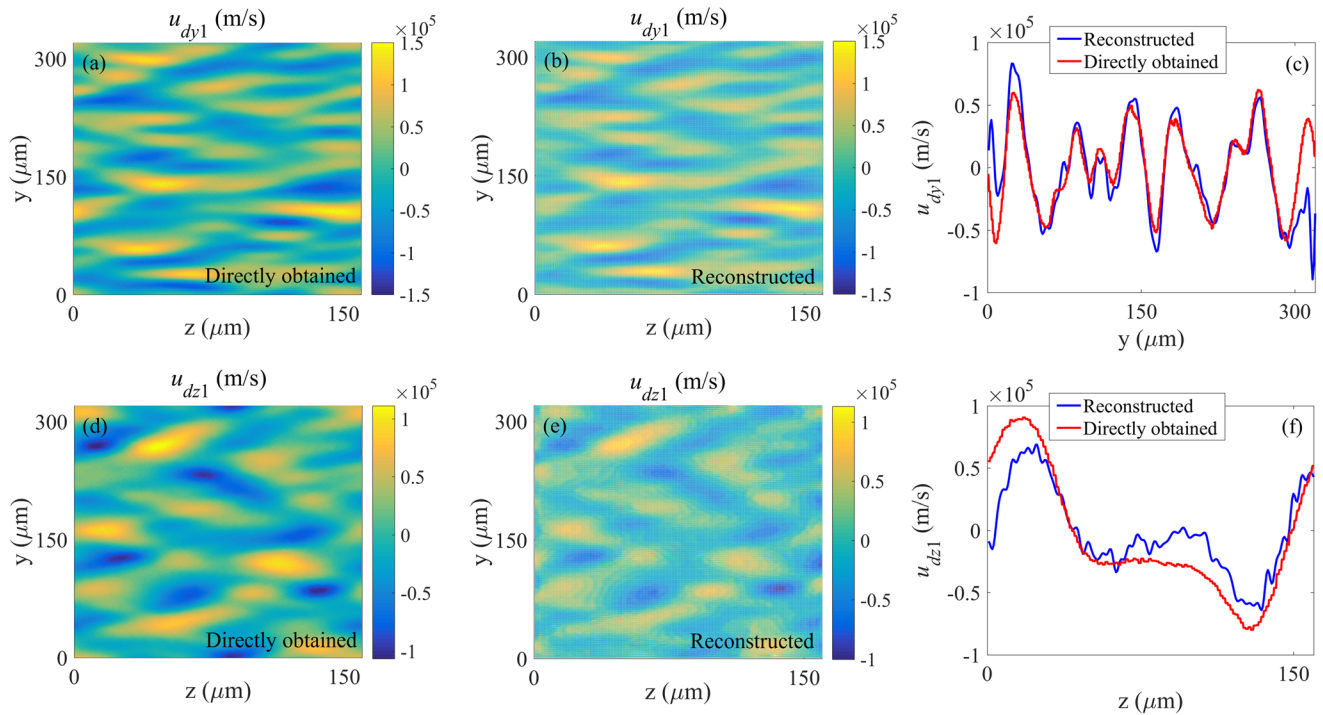

FIG. 8. Deflection velocities for proton beams of kinetic energy $\varepsilon_{k1} = 20$ MeV. (a) u_{dy1} directly obtained from radiography. (b) u_{dy1} reconstructed from $(\delta n/n_0)_1$ in Fig. 7(a). (c) 1D comparison along $z = 80$ μm. (d) Directly obtained u_{dz1}. (e) Reconstructed u_{dz1}. (f) 1D comparison along $y = 160$ μm.
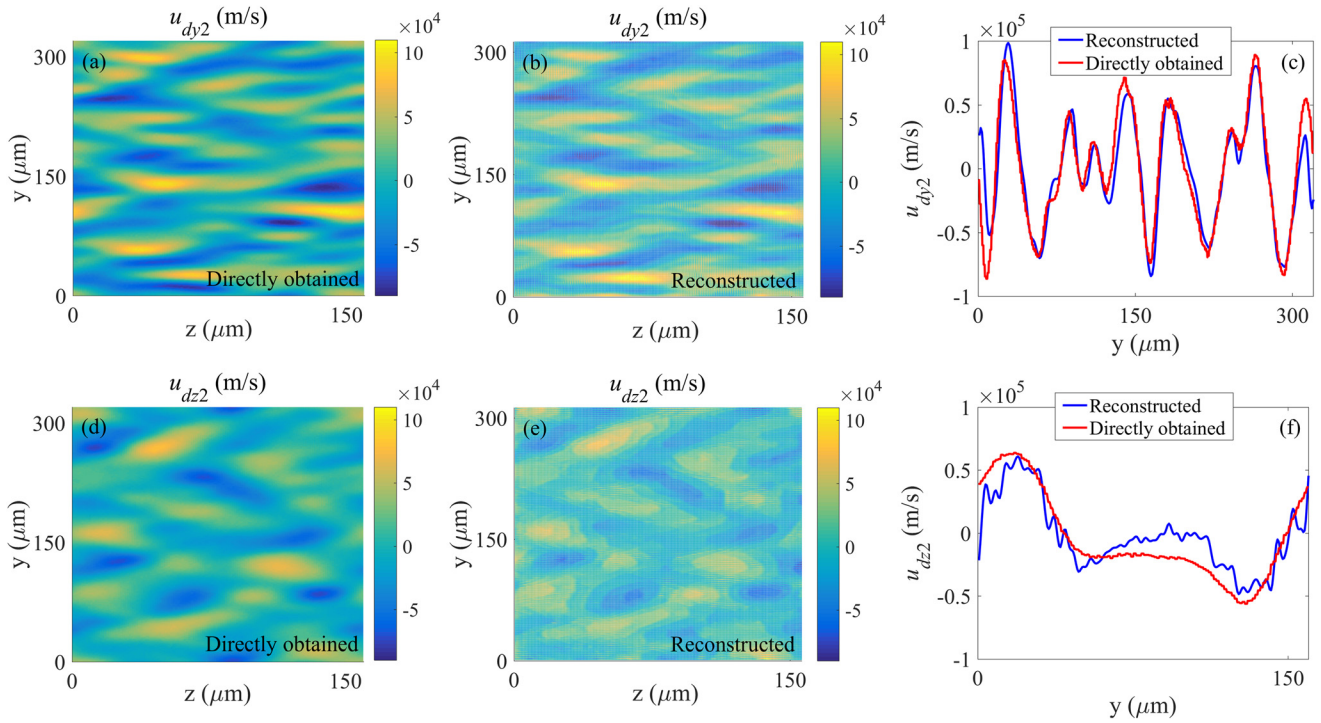
FIG. 9. Deflection velocities for proton beams of kinetic energy ε_{k2} = 40 MeV. (a) u_{dy2} directly obtained from radiography. (b) u_{dy2} reconstructed from $(\delta n/n_0)_2$ in Fig. 7(b). (c) 1D comparison along $z = 80$ μm. (d) Directly obtained u_{dz2}. (e) Reconstructed u_{dz2}. (f) 1D comparison along $y = 160$ μm.
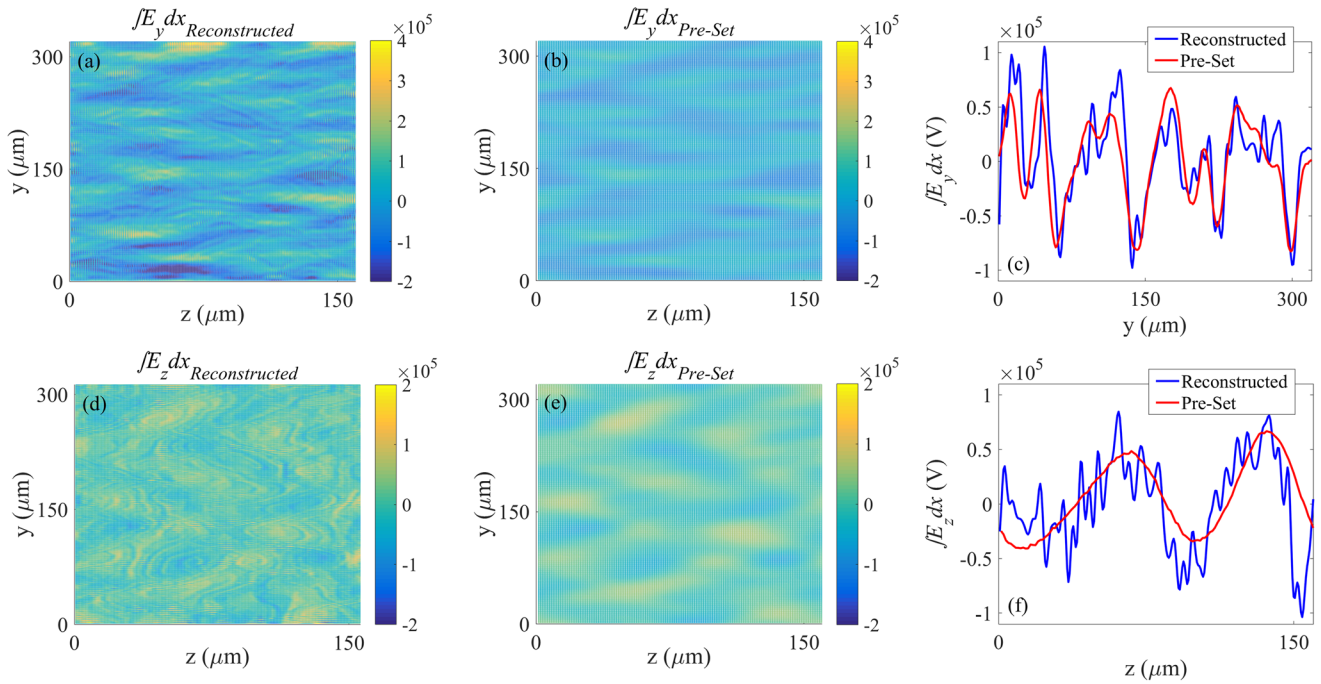

FIG. 10. Comparison of $\int E_y \, dx$: (a) reconstructed from proton radiography; (b) directly obtained from PIC simulation; (c) 1D comparison along $z = 44$ μm. Comparison of $\int E_z \, dx$: (d) reconstructed from proton radiography; (e) directly obtained from PIC simulation; (f) 1D comparison along $y = 88$ μm.

can be compared with the results directly obtained from PIC simulation, as shown in Fig. 11. However, both 2D and 1D comparisons suggest that the reconstructed results are very different from those obtained from PIC simulation. The distributions in Figs. 11(a) and 11(d) indicate that the reconstructed $\int B \, dx$ exhibit no characteristic spatial structures. They are more likely to be stochastically distributed as noise.

In the above analyses, with the same reconstruction methods and $\delta n/n_0$ in the detection plane, the reconstructed $\int E \, dx$ matches well with the pre-set one, but for the B field, the reconstructed path integral differs greatly from the pre-set one and is only at a noise level. This is mainly because in proton radiography, the E field greatly dominates the B field in deflecting the probe protons, as can be seen from Fig. 12, in which the blue and red lines are path integrals of E and $u_0 \times B$, respectively, that have been directly obtained from PIC simulations. Here, $u_0 = u_0 e_x$ is the initial velocity of a proton beam in the x direction with kinetic energy 20 MeV. As a result, when subtracting Eq. (2) from Eq. (3), $u_0 \times B$ cannot even compete with the numerical errors in E. Performing such a subtraction will lead to a reconstructed $\int u_0 \times B \, dx$ that actually consists mainly of numerical errors in $\int E \, dx$ and is stochastically distributed as noise, as can be witnessed in Figs. 11(a) and 11(d).

This also can be inferred by analyzing the uncertainty in the reconstruction. Since few assumptions are made in deriving Eqs. (4) and (5), it is reasonable to focus our attention on the uncertainties in the deflection velocities. In Figs. 8 and 9, the root mean square uncertainties in the 2D u_{dy1}, u_{dz1}, u_{dy2}, and u_{dz2} between the reconstruction and the

pre-set simulations are $S_{uy1} = 1.25 \times 10^4$ m/s, $S_{uz1} = 1.44 \times 10^4$ m/s, $S_{uy2} = 0.94 \times 10^4$ m/s, and $S_{uz2} = 1.06 \times 10^4$ m/s, respectively. In calculating the uncertainties in u_d, regions of width about 6 μm near the boundaries, i.e., $y = 0$ and $y = 316$ μm, $z = 0$ and $z = 158$ μm, are excluded to avoid the numerical errors generated in solving the Monge–Ampère equation.[14] From an error transport analyses of Eqs. (4) and (5), the uncertainties in the reconstructed $\int E_y \, dx$ and $\int E_z \, dx$ can be obtained from $S_{uy,uz}$ as $S_{Ey} = 3.42 \times 10^4$ V and $S_{Ez} = 3.91 \times 10^4$ V, which are smaller than the absolute values of the pre-set fields in Fig. 10. However, for the magnetic fields, the uncertainties in $\int B_y \, dx$ and $\int B_z \, dx$ are obtained as $S_{By} = 4.53 \times 10^{-4}$ T m and $S_{Bz} = 5.16 \times 10^{-4}$ T m, which are much larger than the absolute values of the pre-set fields in Figs. 11(c) and 11(f). This indicates that the reconstructed magnetic fields in Figs. 11(a) and 11(d) are mainly noise produced in the reconstruction, rather than the real distributions.

In general, the deflection velocities in Figs. 9(c) and 9(f) and Figs. 10(c) and 10(f) can be recognized as reconstructed well when compared with the real pre-set ones. Nevertheless, in distinguishing the E and B fields from an experiment, when one of the two fields is greatly dominant in deflecting the probe protons, the above analyses have shown that a high-resolution reconstruction of the deflection velocities is desired. However, this requirement is quite difficult using currently available technology. As a consequence, when using the above method, a user needs an estimate of uncertainty to assess whether the features observed in a reconstruction are real, and, before that, the possible reasons for the bulk of the uncertainty in the reconstruction must be confirmed.
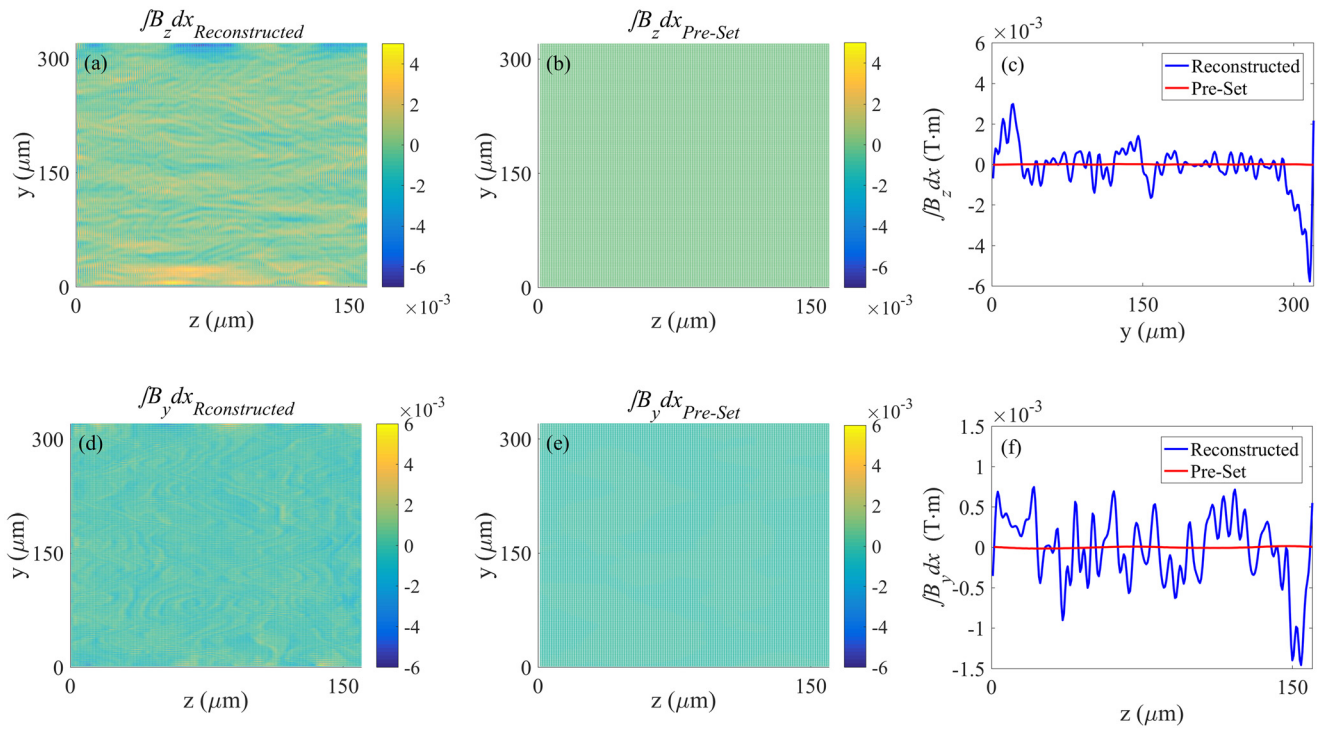

FIG. 11. Comparison of $\int B_z \, dx$: (a) reconstructed from proton radiography; (b) directly obtained from PIC simulation; (c) 1D comparison along $z = 44$ μm. Comparison of $\int B_y \, dx$: (d) reconstructed from proton radiography; (e) directly obtained from PIC simulation; (f) 1D comparison along $y = 88$ μm.
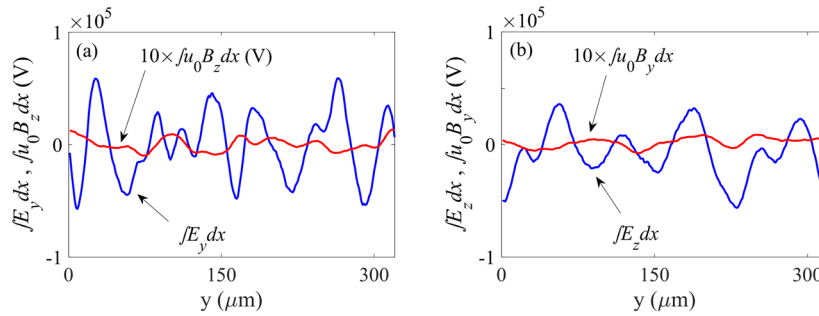
FIG. 12. $\int \boldsymbol{E}\, dx$ and $\int \boldsymbol{u}_0 \times \boldsymbol{B}\, dx$ directly obtained from PIC simulation in (a) the y and (b) the z direction along $z = 80\ \mu m$, in which the amplitudes of $\int \boldsymbol{u}_0 \times \boldsymbol{B}\, dx$ have been amplified by a factor of 10. These results indicate that the $\boldsymbol{E}$ field greatly dominates the $\boldsymbol{B}$ field in deflecting the probe protons.

According to Ref. 14, in proton radiography with parallel beams, when solving the Monge–Ampère equation for $\delta n/n_0$ to reconstruct the deflection velocity, two of the most important equations are[14]

$$r_\perp \approx r_{\perp 0} + \frac{u_d}{u_0} L_D, \tag{12}$$

$$n \approx \frac{n_0}{\left| \dfrac{\partial(y,z)}{\partial(y_0,z_0)} \right|}, \tag{13}$$

where $\boldsymbol{r}_{\perp 0} = \boldsymbol{y}_0 + \boldsymbol{z}_0$ and $\boldsymbol{r}_\perp = \boldsymbol{y} + \boldsymbol{z}$ are the transverse positions of the probe protons in the object and image planes, and $\partial(y,z)/\partial(y_0,z_0)$ is the Jacobian matrix mapping a surface element in the object plane to the surface element in the image plane. In the derivation of Eq. (12) for a parallel probe, the major approximation is that the passage time of the probe protons in the field region is short to ensure that the transverse deflection does not cause any apparent transverse displacement. In other words, the transverse positions of the probe protons on their entry to the field region are approximately the same as those at their exit, i.e., $\Delta r_\perp / r \ll 1$. The uncertainty in transverse positions can be approximated as $S_r \approx l_x u_d / u_0$, where l_x is the length of the field region along the x direction. From the reconstructed u_d in Figs. 8 and 9, S_r is estimated to be about 0.24 μm in our simulation, which is much smaller than the grid length of the imaged field and can be excluded in the resulting S_u. In the derivation of Eq. (13), the major approximation is that the deflection angle u_d/u_0 is so small that no caustic can occur and the trajectories of the probe protons do not overlap or cross, which guarantees a positive Jacobian determinant $\partial(y,z)/\partial(y_0,z_0)$. It is difficult to analyze directly how much influence the assumption of the no-caustic approximation could have on Eq. (13): the no-caustic approximation is not a simplification of Eq. (13) in which some small terms are simply neglected. However, in a 1D case where only one component is considered (we take the y component here, without loss of generality), $n \approx n_0/|1 + \nabla_y d_y|$, where $\nabla_y d_y = \partial(u_d L_D/u_0)/\partial y$. If the transverse displacement $\Delta(u_d L_D/u_0)$ caused by the deflection velocity equals the distance between two nearby probe protons, $-\Delta y$, this means that the trajectories of the two particles overlap or cross. This leads to an infinite proton flux on the detection plane and should be avoided in radiography.

However, using Eq. (13), it is difficult to quantitatively estimate the severity of the trajectory overlapping or crossing. Nevertheless, we notice

that as the deflection is weak, $n \approx n_0/|1 + \nabla_y d_y|$ can be expand as $n \approx n_0(1 - \nabla_y d_y)$, or

$$\delta n \approx -n_0 \nabla_y d_y. \tag{14}$$

Actually, Eq. (14) is the reason why Eqs. (6) and (7) are reasonable expressions, and it has been deduced previously in Refs. 12 and 19 from the equation of continuity $\partial n/\partial t + \nabla_y(n u_d) = 0$, where $t = L_D/u_0$. This can be written as $\delta n + n\nabla_y d_y + d_y \nabla_y n = 0$, which reduces to Eq. (14) when the last term $d_y \nabla_y n$, is neglected, where $d_y = -\int \delta n/n_0\, dy$. As a result, when the deflection velocity is reconstructed from $\delta n/n_0$, the presence of $d_y \nabla_y n$ would cause an uncertainty. The uncertainty in $\delta n/n_0$ in Eq. (14) is then $S_{\delta n} = d_y \nabla_y n/n_0$. According to $d_y = -\int \delta n/n_0\, dy$ and $u_d = u_0 d_y/L_D$, error transport analysis gives the uncertainly in the deflection velocity as

$$S_{ud} = \frac{u_0}{L_D} \frac{\delta n}{\nabla_y(\delta n)} S_{\delta n}. \tag{15}$$

S_{ud} can be regarded as the uncertainty in the reconstructed deflection velocity caused by the no-caustic assumption in the above reconstruction method. However, we should mention that Eq. (15) is based on a 1D analyses. In the 2D case,

$$\frac{\partial(y,z)}{\partial(y_0,z_0)} = (1 + \nabla_y d_y)(1 + \nabla_z d_z) - (\nabla_z d_y)(\nabla_y d_z).$$

In this case, it is much too complicated to estimate how exactly the equation of continuity can be approximated to give Eq. (14). However, it is certain that in the 2D case, the uncertainty in the reconstruction will be larger according to the law of error transport. As an approximation, we can still use Eq. (14) to estimate the uncertainties of the reconstructed deflection velocities.

With Eq. (15) and $\delta n/n_0$ in Fig. 7, for 20 MeV protons, the uncertainties are obtained as $S'_{uy1} = 1.15 \times 10^4$ m/s and $S'_{uz1} = 0.84 \times 10^4$ m/s, whereas for 40 MeV protons, they are obtained as $S'_{uy2} = 0.77 \times 10^4$ m/s and $S'_{uz2} = 0.68 \times 10^4$ m/s. In comparison with those obtained by directly counting from Figs. 8 and 9, the S'_u are quite close to S_u, which indicates the applicability of Eq. (15). The differences possibly result from multidimensional effects in evaluating $\delta n/n_0$, as has already been discussed. This analysis indicates that the no-caustic approximation could be the major reason for the uncertainties in reconstruction. Furthermore, it suggests that to achieve reconstruction of $\boldsymbol{E}$

and **B** fields with low uncertainties, appropriate distances from the source and detector to the field region should been used in future experimental applications to avoid caustics in the proton trajectories.

VI. CONCLUSION

Using theoretical analyses and numerical simulations, we have demonstrated a method to distinguish the contributions of **E** and **B** fields in deflecting probe protons in proton radiography when both fields coexist. By using RCF stacks or CR-39 polymer as proton detectors to resolve the proton energy, path integrals of the **E** and **B** fields can be separately reconstructed from the flux distributions of protons with two discriminated energies in a single radiography observation. A method has also been proposed for eliminating the influence of field evolution on the separation and has been proved to be viable. The method demonstrated in this paper could be helpful in understanding and more rigorously analyzing proton flux distributions in proton radiography experiments.

ACKNOWLEDGMENTS

REFERENCES

[1]C. K. Li, F. H. Séguin, J. A. Frenje, M. Rosenberg, R. D. Petrasso, P. A. Amendt, J. A. Koch, O. L. Landen, H. S. Park, H. F. Robey, R. P. J. Town, A. Casner, F. Philippe, R. Betti, J. P. Knauer, D. D. Meyerhofer, C. A. Back, J. D. Kilkenny, and A. Nikroo, "Charged-particle probing of X-ray-driven inertial-fusion implosions," Science **327**, 1231 (2010).

[2]C. M. Huntington, F. Fiuza, J. S. Ross, A. B. Zylstra, R. P. Drake, D. H. Froula, G. Gregori, N. L. Kugland, C. C. Kuranz, M. C. Levy, C. K. Li, J. Meinecke, T. Morita, R. Petrasso, C. Plechaty, B. A. Remington, D. D. Ryutov, Y. Sakawa, A. Spitkovsky, H. Takabe, and H.-S. Park, "Observation of magnetic field generation via the Weibel instability in interpenetrating plasma flows," Nat. Phys. **11**, 173 (2015).

[3]A. Macchi, M. Borghesi, and M. Passoni, "Ion acceleration by superintense laser-plasma interaction," Rev. Mod. Phys. **85**, 751 (2013).

[4]N. L. Kugland, D. D. Ryutov, P.-Y. Chang, R. P. Drake, G. Fiksel, D. H. Froula, S. H. Glenzer, G. Gregori, M. Grosskopf, M. Koenig, Y. Kuramitsu, C. Kuranz, M. C. Levy, E. Liang, J. Meinecke, F. Miniati, T. Morita, A. Pelka, C. Plechaty, R. Presura, A. Ravasio, B. A. Remington, B. Reville, J. S. Ross, Y. Sakawa, A. Spitkovsky, H. Takabe, and H.-S. Park, "Self-organized electromagnetic field structures in laser-produced counter-streaming plasmas," Nat. Phys. **8**, 809 (2012).

[5]K. Quinn, L. Romagnani, B. Ramakrishna, G. Sarri, M. E. Dieckmann, P. A. Wilson, J. Fuchs, L. Lancia, A. Pipahl, T. Toncian, O. Willi, R. J. Clarke, M. Notley, A. Macchi, and M. Borghesi, "Weibel-induced filamentation during an ultrafast laser-driven plasma expansion," Phys. Rev. Lett. **108**, 135001 (2012).

[6]C. K. Li, F. H. Séguin, J. A. Frenje, J. R. Rygg, R. D. Petrasso, R. P. J. Town, P. A. Amendt, S. P. Hatchett, O. L. Landen, A. J. Mackinnon, P. K. Patel, V. A. Smalyuk, T. C. Sangster, and J. P. Knauer, "Measuring E and B fields in laser-produced plasmas with monoenergetic proton radiography," Phys. Rev. Lett. **97**, 135003 (2006).

[7]C. K. Li, P. Tzeferacos, D. Lamb, G. Gregori, P. A. Norreys, M. J. Rosenberg, R. K. Follett, D. H. Froula, M. Koenig, F. H. Séguin, J. A. Frenje, H. G. Rinderknecht, H. Sio, A. B. Zylstra, R. D. Petrasso, P. A. Amendt, H. S. Park, B. A. Remington, D. D. Ryutov, S. C. Wilks, R. Betti, A. Frank, S. X. Hu, T. C. Sangster, P. Hartigan, R. P. Drake, C. C. Kuranz, S. V. Lebedev, and N. C. Woolsey, "Scaled laboratory experiments explain the kink behaviour of the Crab Nebula jet," Nat. Commun. **7**, 13081 (2016).

[8]L. Gao, E. Liang, Y. Lu, R. K. Follet, H. Sio, P. Tzeferacos, D. H. Froula, A. Birkel, C. K. Li, D. Lamb, R. Petrasso, W. Fu, M. Wei, and H. Ji, "Mega-Gauss plasma jet creation using a ring of laser beams," Astrophys. J. Lett. **873**, L11 (2019).

[9]P. M. Nilson, L. Willingale, M. C. Kaluza, C. Kamperidis, S. Minardi, M. S. Wei, P. Fernandes, M. Notley, S. Bandyopadhyay, M. Sherlock, R. J. Kingham, M. Tatarakis, Z. Najmudin, W. Rozmus, R. G. Evans, M. G. Haines, A. E. Dangor, and K. Krushelnick, "Magnetic reconnection and plasma dynamics in two-beam laser-solid interactions," Phys. Rev. Lett. **97**, 255001 (2006).

[10]J. R. Rygg, F. H. Séguin, C. K. Li, J. A. Frenje, M. J.-E. Manuel, R. D. Petrasso, R. Betti, J. A. Delettrez, O. V. Gotchev, J. P. Knauer, D. D. Meyerhofer, F. J. Marshall, C. Stoeckl, and W. Theobald, "Proton radiography of inertial fusion implosions," Science **319**, 1223 (2008).

[11]C. J. Zhang, J. F. Hua, Y. Wan, C. H. Pai, B. Guo, J. Zhang, Y. Ma, F. Li, Y. P. Wu, H. H. Chu, Y. Q. Gu, X. L. Xu, W. B. Mori, C. Joshi, J. Wang, and W. Lu, "Femtosecond probing of plasma wakefields and observation of the plasma wake reversal using a relativistic electron bunch," Phys. Rev. Lett. **119**, 064801 (2017).

[12]C. J. Zhang, J. F. Hua, X. L. Xu, F. Li, C. H. Pai, Y. Wan, Y. P. Wu, Y. Q. Gu, W. B. Mori, C. Joshi, and W. Lu, "Capturing relativistic wakefield structures in plasmas using ultrashort high-energy electrons as a probe," Sci. Rep. **6**, 29485 (2016).

[13]N. L. Kugland, D. D. Ryutov, C. Plechaty, J. S. Ross, and H.-S. Park, "Relation between electric and magnetic field structures and their proton-beam images," Rev. Sci. Instrum. **83**, 101301 (2012).

[14]A. F. A. Bott, C. Graziani, P. Tzeferacos, T. G. White, D. Q. Lamb, G. Gregori, and A. A. Schekochihin, "Proton imaging of stochastic magnetic fields," J. Plasma Phys. **83**, 905830614 (2017).

[15]R. Castriconi, M. Ciocca, A. Mirandola, C. Sini, S. Broggi, M. Schwarz, F. Fracchiolla, M. Martišíková, G. Aricò, G. Mettivier, and P. Russo, "Dose-response of EBT3 radiochromic films to proton and carbon ion clinical beams," Phys. Med. Biol. **62**, 377 (2017).

[16]B. Du, H.-B. Cai, W.-S. Zhang, J.-M. Tian, E.-H. Zhang, S.-Y. Zou, J. Chen, and S.-P. Zhu, "Distinguishing and diagnosing the spontaneous electric and magnetic fields of Weibel instability through proton radiography," Plasma Phys. Control. Fusion **62**, 025017 (2020).

[17]J. Matteucci, W. Fox, A. Bhattacharjee, D. B. Schaeffer, C. Moissard, K. Germaschewski, G. Fiksel, and S. X. Hu, "Biermann-battery-mediated magnetic reconnection in 3D colliding plasmas," Phys. Rev. Lett. **121**, 095001 (2018).

[18]W. Wang, H. Cai, J. Teng, J. Chen, S. He, L. Shan, F. Lu, Y. Wu, B. Zhang, W. Hong, B. Bi, F. Zhang, D. Liu, F. Xue, B. Li, H. Liu, W. He, J. Jiao, K. Dong, F. Zhang, Y. He, B. Cui, N. Xie, Z. Yuan, C. Tian, X. Wang, K. Zhou, Z. Deng, Z. Zhang, W. Zhou, L. Cao, B. Zhang, S. Zhu, X. He, and Y. Gu, "Efficient production of strong magnetic fields from ultraintense ultrashort laser pulse with capacitor-coil target," Phys. Plasmas **25**, 083111 (2018).

[19]B. Du and X.-F. Wang, "Prevention of trajectory crossings in proton radiography and the reconstruction of a sheath electric field," AIP Adv. **8**, 125328 (2018).

[20]A. Higginson, R. J. Gray, M. King, R. J. Dance, S. D. R. Williamson, N. M. H. Butler, R. Wilson, R. Capdessus, C. Armstrong, J. S. Green, S. J. Hawkes, P. Martin, W. Q. Wei, S. R. Mirfayzi, X. H. Yuan, S. Kar, M. Borghesi, R. J. Clarke, D. Neely, and P. McKenna, "Near-100 MeV protons via a laser-driven transparency-enhanced hybrid acceleration scheme," Nat. Commun. **9**, 724 (2018).

[21]A. B. Zylstra, C. K. Li, H. G. Rinderknecht, F. H. Séguin, R. D. Petrasso, C. Stoeckl, D. D. Meyerhofer, P. Nilson, T. C. Sangster, S. Le Pape, A. Mackinnon, and P. Patel, "Using high-intensity laser-generated energetic protons to radiograph directly driven implosions," Rev. Sci. Instrum. **83**, 013511 (2012).

[22]L. Q. Shan, H. B. Cai, W. S. Zhang, Q. Tang, F. Zhang, Z. F. Song, B. Bi, F. J. Ge, J. B. Chen, D. X. Liu, W. W. Wang, Z. H. Yang, W. Qi, C. Tian, Z. Q. Yuan, B. Zhang, L. Yang, J. L. Jiao, B. Cui, W. M. Zhou, L. F. Cao, C. T. Zhou, Y. Q. Gu, B. H. Zhang, S. P. Zhu, and X. T. He, "Experimental evidence of kinetic effects in

indirect-drive inertial confinement fusion hohlraums," Phys. Rev. Lett. **120**, 195001 (2018).

[23]F. H. Séguin, C. K. Li, M. J.-E. Manuel, H. G. Rinderknecht, N. Sinenian, J. A. Frenje, J. R. Rygg, D. G. Hicks, R. D. Petrasso, J. Delettrez, R. Betti, F. J. Marshall, and V. A. Smalyuk, "Time evolution of filamentation and self-generated fields in the coronae of directly driven inertial-confinement fusion capsules," Phys. Plasmas **19**, 012701 (2012).

[24]M. J.-E. Manuel, C. K. Li, F. H. Séguin, N. Sinenian, J. A. Frenje, D. T. Casey, R. D. Petrasso, J. D. Hager, R. Betti, S. X. Hu, J. Delettrez, and D. D. Meyerhofer, "Instability-driven electromagnetic fields in coronal plasmas," Phys. Plasmas **20**, 056301 (2013).

[25]L. Gao, P. M. Nilson, I. V. Igumenshchev, M. G. Haines, D. H. Froula, R. Betti, and D. D. Meyerhofer, "Precision mapping of laser-driven magnetic fields and their evolution in high-energy-density plasmas," Phys. Rev. Lett. **114**, 215003 (2015).